

# Influence of Very High-Frequency PECVD Hydrogen Plasma Treatment on Intrinsic Amorphous Silicon Passivation Stack: Impact on Silicon Heterojunction Solar Cell Performance

Ashutosh Pandey, Shrestha Bhattacharya, Shahnawaz Alam, Silajit Manna, Sourav Sadhukhan, Son Pal Singh, and Vamsi Krishna Komarala\*



Cite This: ACS Appl. Energy Mater. 2025, 8, 366–375



Read Online

ACCESS |

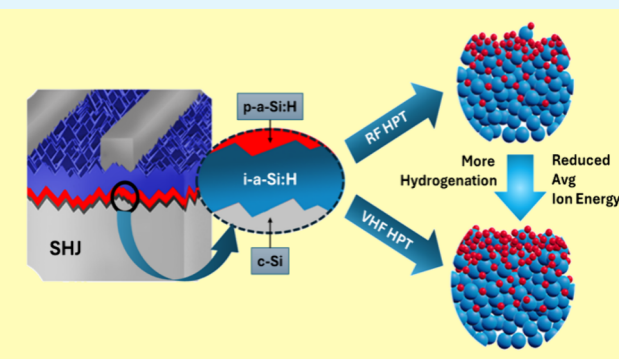
Metrics & More

Article Recommendations

Supporting Information

**ABSTRACT:** We have investigated the impact of post hydrogen plasma treatment (HPT) using two distinct RF generators operating at 13.56 and 40.68 MHz on the PECVD-deposited i-a-Si:H bilayer stack. VHF-HPT (40.68 MHz) improved the film microstructure, reducing the void fraction to ~29.9%, compared to ~34.5% for RF-HPT (13.56 MHz). Consequently, VHF-HPT led to the enhanced minority carrier lifetime to ~2.7 ms, thereby improving silicon heterojunction solar cell power conversion efficiency to ~21.31% with an open-circuit voltage of ~733 mV. In-situ optical emission spectra study of H<sub>2</sub> plasma indicated modification in H ions/radicals intensity, which led to enhanced film density and reduced film thickness, further confirmed by spectroscopic ellipsometry analysis. Along with better passivation after VHF-HPT, the hole-selective contact resistivity is also reduced to ~278 mΩ·cm<sup>2</sup> compared to the RF-HPT treatment having ~378 mΩ·cm<sup>2</sup>. Dark J-V analysis of cells using a two-diode model revealed that the ideality factor reduced significantly for VHF-HPT, indicating reduced recombination in the space charge region. Finally, the experimental observations are also validated by Sentaurus TCAD numerical simulations by considering i-a-Si:H bulk and c-Si/i-a-Si:H interface defect densities.

**KEYWORDS:** hydrogenated amorphous silicon, interfacial passivation, hydrogen plasma treatment, very-high frequency plasma, silicon heterojunction solar cell



## 1. INTRODUCTION

The silicon heterojunction (SHJ) solar cells have drawn great attention in the photovoltaic research area along with the crystalline silicon-based high-efficiency TOPCon cells due to high open-circuit voltage ( $V_{oc}$ ) and better temperature coefficient under the standard test conditions.<sup>1</sup> Moreover, flexible solar cells are also an emerging trend in photovoltaics, offering lightweight, durable solutions for diverse applications like BIPV and wearables.<sup>2</sup> Hydrogenated intrinsic and doped amorphous silicon (a-Si:H) layers are deposited using a plasma-enhanced chemical vapor deposition (PECVD) tool, which is employed in SHJ cell fabrication for the c-Si surface passivation and carrier-selective contacts. Hot-wire chemical vapor deposition (HWCVD) and sputtering methods have also been employed to deposit hydrogenated intrinsic and doped amorphous silicon layers, primarily because of their high deposition rates.<sup>3,4</sup> The efficiency of SHJ solar cells is constrained by recombination losses at the c-Si surface (apart from some band offsets at the hole- and electron-selective layers), making effective surface passivation crucial for minimizing such losses.<sup>5,6</sup> Hydrogen is widely used in

semiconductor processing, especially in amorphous and microcrystalline silicon thin films for suppressing unwanted dangling bonds during film growth along with restructuring the film's microstructure for solar cell performance enhancement. Due to its low mass, hydrogen can readily diffuse through the amorphous silicon network, effectively passivating silicon dangling bonds and contributing to the stabilization of metastable defects.<sup>7</sup>

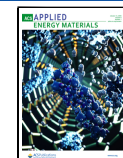
The importance of hydrogen plasma treatment (HPT) in SHJ cells has been identified for enhancing the c-Si surface passivation and reducing the photogenerated charge carrier recombination losses to improve the cells' overall efficiency. The HPT prior to the a-Si:H deposition was investigated to effectively passivate the c-Si surface dangling bonds by

Received: September 28, 2024

Revised: December 19, 2024

Accepted: December 23, 2024

Published: January 2, 2025



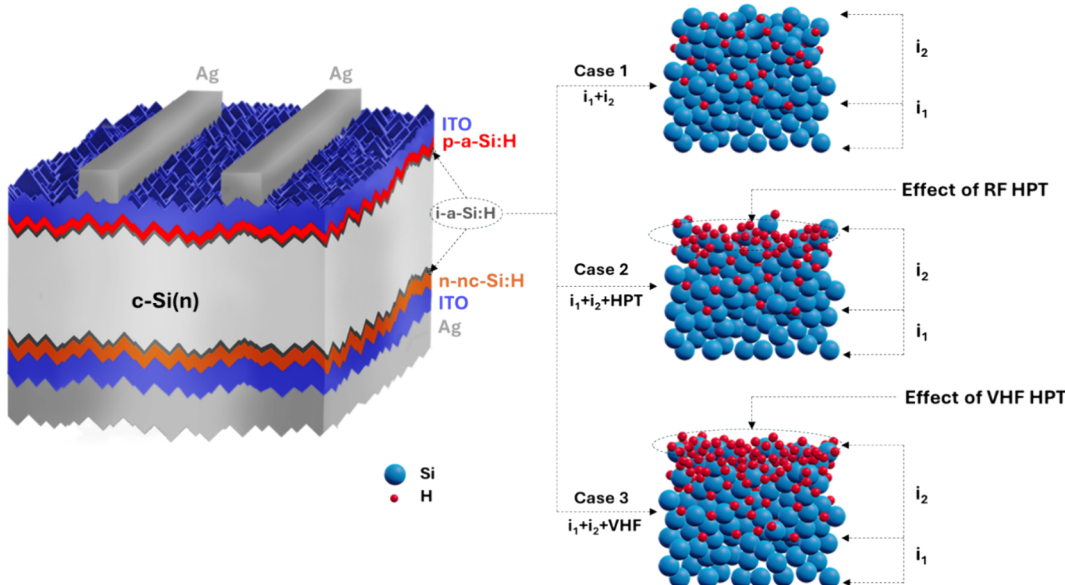


**Figure 1.** Schematic of fabricated SHJ cell structure (left), highlighting the three i-a-Si:H passivation layer stacks (right): (Case 1) only bilayer stack, (Case 2) bilayer stack with RF-HPT, and (Case 3) bilayer stack with VHF-HPT conditions.

reducing recombination-active defects.<sup>8,9</sup> Besides, the effect of HPT not only prior to the i-layer deposition but also after each intrinsic a-Si:H layer deposition and before the doped layer deposition in the SHJ solar cells has been studied.<sup>7,10</sup> To further improve the c-Si surface passivation and mitigate any adverse effect, it is essential to fine-tune deposition conditions of the a-Si:H; such as hydrogen dilution ratio ( $\text{SiH}_4/\text{H}_2$ ), deposition pressure, applied power density, and residence time of dissociated radicals to promote the formation of  $\text{SiH}_3$  radicals.<sup>11</sup> Additionally, methods like the use of multilayers with variable microstructure i-a-Si:H layers, pre/post- and intermediate-HPT, postannealing, and utilizing a multilayer approach have already been explored by the researchers to enhance the c-Si surface chemical passivation.<sup>12–15</sup> An effective strategy to devise the passivation using distinct steps in which, first, a low-mass-density (porous) a-S:H film is deposited onto the textured c-Si surface to prevent epitaxy and achieve an abrupt a-S:H/c-Si interface, followed by the HPT to furnish the H atoms into the high-defect-density a-Si/c-Si interface, effectively reducing the surface recombination velocity (SRV) at the interface.<sup>7</sup>

The HPT generated at the lower frequency plasma typically has a lower plasma density distribution, and also, hydrogen atoms available might be less uniform, leading to inconsistent passivation across the silicon surface.<sup>16</sup> Thus, the HPT treatment at higher plasma frequency has become a promising aspect for many research groups.<sup>17</sup> It is quite well-known that as the excitation frequency increases, the plasma sheath field decreases, leading to a reduction in ion energy.<sup>18</sup> This reduced ion bombardment during plasma treatment can be beneficial as it would produce enough kinetic energy for the H atoms to diffuse, thus passivating the silicon dangling bonds and also, at the same time, prevent defect formation or bond rupture due to higher ion energy at plasma generated at low frequencies.<sup>16,18,19</sup>

The presence of defects at any interface can induce an unwanted leakage current path in an SHJ cell, which is evaluated by the recombination current density ( $J_0$ ). Generally, the summation of all the recombination activity in the emitter,

bulk, and rear part regions can be lumped together as the  $J_0$  in a cell. The fill factor of an SHJ solar cell is also significantly influenced by the  $J_0$  along with cell ohmic resistances.<sup>20</sup> One can realize high power conversion efficiency from an SHJ cell by balancing the charge carrier recombination and transport. In this regard,  $J_0$  is an important parameter that needs to be addressed carefully to improve and design more efficient cells.<sup>21</sup> Further, to understand the impact of  $J_0$ , the two-diode model of solar cells is employed<sup>22</sup>;  $J_{01}$  accounts for recombination currents within the quasi-neutral bulk and at cell surfaces, and  $J_{02}$  is associated with the Shockley-Read-Hall (SRH) recombination occurring in the space charge regions of a cell.<sup>20,23</sup>

Thus, VHF-HPT can be an option to tune the microstructure of the i-a-S:H layer and improve the c-Si surface passivation to achieve better device performance. However, the potential of VHF-based HPT for SHJ cells has not been explored much regarding surface defect minimization. In this study, we tried to demonstrate the modification in dual i-a-Si:H layers using HPT at different frequencies (13.56 and 40.68 MHz). SHJ cells are also fabricated without and with HPT treatment to understand the cell's photovoltaic parameters; we have observed the importance of VHF-HPT treatment on cells' open-circuit voltage (from ~705 to ~733 mV) and fill factor (~71.64 to ~75.20%) enhancement and overall cell power conversion efficiency from ~19 to ~21%. Also, a three-dimensional simulation was carried out using the Sentaurus TCAD tool, considering the material properties and layer dimensions of the fabricated SHJ cells. The simulation primarily focused on investigating the passivation of the intrinsic layer by varying defect states both in the bulk and at the surfaces, explaining the improvement by VHF-HPT.

## 2. EXPERIMENTAL DETAILS

The front emitter SHJ cells, as shown in the schematic (Figure 1), were fabricated from an as-cut Cz monocrystalline silicon wafer (~120  $\mu\text{m}$  thickness and resistivity of 4–5  $\Omega\text{-cm}$ ). The silicon surface was prepared using the standard cleaning procedure, which includes piranha cleaning, saw damage removal (SDR), texturization, pyramid smoothing, and RCA1 and RCA2 steps. The wafers were textured in

~2 wt % KOH- mono-TEX additive to obtain a random pyramid size of ~2  $\mu\text{m}$  on both sides of the c-Si wafer. The peaks and valleys of the obtained pyramids were polished by using an HNA treatment, which includes hydrofluoric acid, nitric acid, and acetic acid.

Postcleaning process followed by ~1% HF dip (for 120 s), the textured wafers were loaded in the capacitively coupled PECVD system from Samco, Japan. This was used to deposit intrinsic a-Si:H passivating layers, boron-doped a-Si:H hole-selective layers, and phosphorus-doped nanocrystalline silicon (nc-Si:H) electron-selective layers. Hydrogen ( $\text{H}_2$ ) and silane ( $\text{SiH}_4$ ) gases were used as the carrier gas for the deposition of the ~8 nm i-a-Si:H layer. Diborane (~3% in  $\text{H}_2$ ) and Phosphine (~4% in  $\text{SiH}_4$ ) gases were used as dopant gases to deposit hole- and electron-selective layers, respectively. To tune the microstructure of the passivating i-a-Si:H layer, the HPT was performed at either radio frequency (RF, 13.56 MHz) or very high frequency (VHF, 40.68 MHz); details are presented in Table 1. The hole-selective p-a-Si:H layer was deposited

**Table 1. PECVD Deposition Parameters of Different Intrinsic Amorphous Silicon Layers and HPT Details with Different Frequencies**

	$i_1$	$i_2$	RF-HPT	VHF-HPT
$\text{SiH}_4/\text{H}_2$ (sccm)	40/0	20/100	0/250	0/250
Pressure (Pa)	50	80	133	133
Power Density (mW/cm <sup>2</sup> )	122	122	306	306
Temperature (°C)	215	215	215	215
Frequency (MHz)	13.56	13.56	13.56	40.68
HPT Duration (s)			14	14

using a 13.56 MHz frequency generator, whereas the nc-Si:H electron-selective layer was deposited using 27.12 MHz with very high hydrogen gas dilution.<sup>24</sup> More details on the amorphous layer optimization can be found in our previous work.<sup>25</sup>

Indium tin oxide (ITO) of ~80 nm was deposited by the RF magnetron sputtering using a 2-in.  $\text{In}_2\text{O}_3$ :  $\text{SnO}_2$  (90:10 wt %) target by varying the oxygen flow into the system at the fixed Argon flow having the mobility of ~40 cm<sup>2</sup>/V-s and carrier concentration of ~2  $\times 10^{20}$  cm<sup>-3</sup>.<sup>26</sup> The cell area was defined with 1.7  $\times$  1.7 cm<sup>2</sup> using a shadow mask for ITO deposition by RF sputtering, followed by the silver grid in the front contact with the surface coverage of 6–7%. The electron-selective side of the SHJ structure was fully covered with ~80 nm ITO and ~1000 nm of Ag films.

The  $J_0$  is estimated from the ~8 nm i-a-Si:H passivating layers with different conditions on both sides of the textured c-Si wafer. The optical emission spectra for the precursor gases of  $\text{SiH}_4$  and/or  $\text{H}_2$  during i-a-Si:H layer deposition were monitored in situ using an Ocean Optics (HDX model) spectrometer. The thickness of different i-a-Si:H layers was measured using spectroscopic ellipsometry by depositing on an n-type single-side polished silicon wafer. The thickness mentioned in this study (on the textured wafer) is the measured thickness on the planar wafer divided by a well-known geometrical factor of 1.73.<sup>27</sup> The minority carrier lifetime (MCL) measurements of the symmetrically passivated samples were carried out using a Sinton Lifetime Tester WCT-120TS instrument to study the passivation. SHJ cells were also fabricated to evaluate the photovoltaic parameters with different i-a-Si:H layers. The indium, oxygen, tin, boron, and silicon concentration profiles with c-Si/i-a-Si:H/p-a-Si:H/TCO were analyzed by the TOF-SIMS (IONTOF GmbH, Germany) and acquired using a 500 eV  $\text{Cs}^+$  sputter beam. The device's current–voltage (J-V) characteristics were determined using a Class AAA solar simulator (Oriel Sol3A, Newport, USA) under standard test conditions of 25 °C and AM1.5G. The  $J_0$  at the device level was also estimated from the cells' light and dark J-V characteristics. The Suns- $V_{oc}$  and the pseudo fill factor (pFF) were estimated from the Sinton Suns- $V_{oc}$  Tester. The experimental observations are supported by 3D numerical simulations of the complete device structure using the Sentaurus TCAD tool.

### 3. RESULTS AND DISCUSSION

The effective MCL ( $\tau_{\text{eff}}$ ) plots of the n-type c-Si wafers passivated with thin i-a-Si:H layers deposited at different conditions are presented in Figure 2. In this graph, the i-layer is

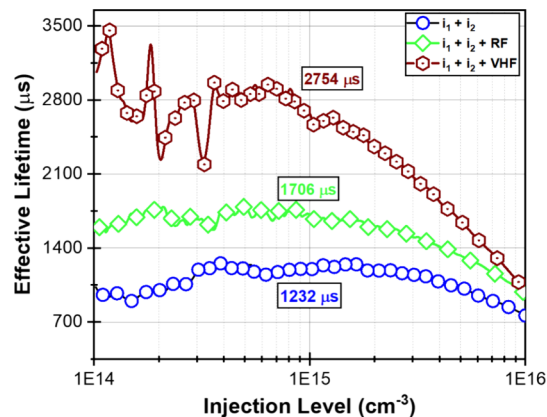


**Figure 2.** Effective minority carrier lifetimes of the n-type c-Si wafer at different carrier injection levels with different passivating i-a-Si:H layers.

modified in the following manner: (a)  $i_1 + i_2$ , where the  $i_1$  layer is deposited with pure silane gas during its processing (underdense) followed by the  $i_2$ -layer deposited with hydrogen diluted silane (dense), (b)  $i_1 + i_2 + \text{HPT}$  with HPT using 13.56 MHz RF plasma after  $i_1 + i_2$  deposition, and (c)  $i_1 + i_2 + \text{VHF}$  with VHF-based HPT using 40.68 MHz plasma. One can clearly observe that the i-a-Si:H layer deposited with  $i_1 + i_2 + \text{VHF}$  shows the highest  $\tau_{\text{eff}}$  for the entire minority charge carrier injection density range. Effective lifetimes of ~1.2–1.7 and ~2.7 ms at a carrier injection level of  $1 \times 10^{15}$  cm<sup>-3</sup> are observed for the c-Si wafers passivated with the  $i_1 + i_2$ ,  $i_1 + i_2 + \text{RF}$ , and  $i_1 + i_2 + \text{VHF}$  layers, respectively.

According to the reported literature, the microstructure of the i-a-Si:H layer is quite crucial for the c-Si surface passivation in addition to the unhindered charge carrier transport toward the respective selective contacts in an SHJ cell.<sup>13</sup> The porous microstructure in the i-a-Si:H layer is necessary to prevent epitaxial crystallization at the c-Si interface, whereas a dense i-a-Si:H layer is also required for better passivation. With this motivation, initially, we used a combination of  $i_1$  and  $i_2$ -a-Si:H layers, optimizing the film's thickness of ~8 nm, and observed  $\tau_{\text{eff}}$  of ~1.2 ms. An improvement in  $\tau_{\text{eff}}$  to ~1.7 ms and ~2.7 ms was observed when the combination of the  $i_1 + i_2$  layer was followed by RF-HPT and VHF-HPT, although the thickness of the  $i_1 + i_2$  stack reduced to <8 nm for the RF-HPT case (details are presented in the next section). In general, HPT helps to increase both the H concentration and the optimum porosity of the bi-intrinsic amorphous layer.<sup>7,10,28</sup> The H radicals during HPT facilitate the c-Si/i-a-Si:H interface with defect reduction by minimizing c-Si dangling bonds, and the H reservoir helps to hydrogenate the bulk i-a-Si:H layers.

During HPTs, enough electrons are generated through primary and secondary plasma collisions, achieving the required energy (~4.52 eV) needed to dissociate hydrogen bonds and produce  $\text{H}^+$  ions along with some neutral  $\text{H}^*$  atoms. Both ions and neutrals move toward the substrate due to the oscillating electric field and enter the plasma sheath. The energy is regulated through collisions with pre-existing positive ions and neutrals in the sheath, resulting in an ion energy

distribution that significantly influences the hydrogen content in the film. The significant improvement in the  $\tau_{\text{eff}}$  with the VHF-HPT can be linked to the reduced plasma sheath impedance, which enables the availability of sufficient ion flux while simultaneously keeping ion energy and electrode voltage at minimal levels.<sup>18</sup> In this way, it helps to lower the hydrogen ion bombardment energy, which modifies the microstructure of the passivating i-a-Si:H layer by providing less damage and controlled etching of a film for optimum porosity in the thin film.

Under illumination, the carrier recombination mechanism varied with the excess carrier density. At lower densities, the defects arising from the bulk and surface/interface defects are mostly dominant, and thus, variation in the  $\tau_{\text{eff}}$ . Photo-generated charge carriers diffuse toward the trap centers, and the probability of recombination increases. The mobility of the generated carriers causes an internal flow of the current, making carrier transport and recombination major issues under illumination. Thus, neglecting the bulk recombination (since we are using a high bulk lifetime c-Si wafers) and considering recombination at lower injection, the  $J_0$  is a crucial parameter that needs to be quantified.<sup>29</sup> The calculation of  $J_0$  is performed using the Kane and Swanson model as used in the Sinton WCT software.<sup>30</sup> In this model, it is assumed that the overall recombination can be expressed by a mathematical relation for each excess carrier concentration ( $\Delta n$ ):

$$\frac{\Delta n}{\tau_{\text{eff}}} = \frac{\Delta n}{\tau_{\text{int}}} + \frac{\Delta n}{\tau_{\text{SRH}}} + \frac{J_0(N_D + \Delta n)\Delta n}{qWn_i^2}$$

Here,  $W$  represents the thickness of the sample,  $N_D$  refers to the base doping concentration,  $n_i$  represents the intrinsic carrier density, and  $\tau_{\text{int}}$  denotes the lifetime associated with radiative and Auger recombination in the base. Figure 3 shows

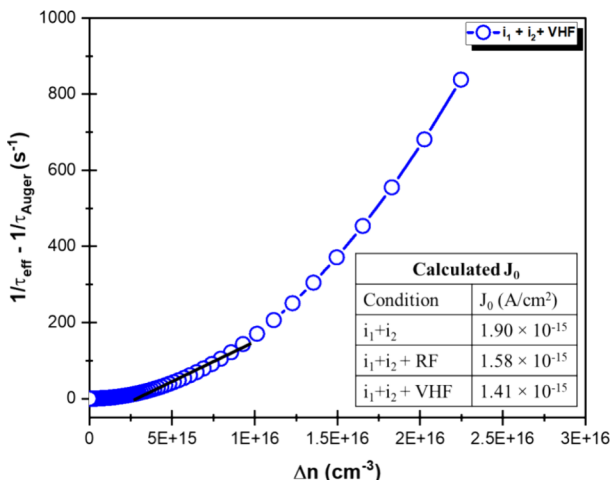


**Figure 3.** Auger corrected  $\tau_{\text{eff}}$  vs  $\Delta n$  plot of the c-Si surface passivated with the  $i_1 + i_2 + \text{VHF}$  layers; extracted  $J_0$  values after linear fitting are presented in the table from all samples as an inset.

the  $J_0$  extraction from the slope of the  $1/\tau_{\text{corr}} = (1/\tau_{\text{eff}} - 1/\tau_{\text{int}})$  vs  $\Delta n$  graph by considering data from  $5 \times 10^{15}$  to  $1 \times 10^{16}$   $\text{cm}^{-3}$  carrier injection.<sup>31</sup> The variation in the  $J_0$  values from 3 samples is shown in the table as an inset of Figure 3. The wafers undergo identical texturization and cleaning processes, so the estimated  $J_0$  for  $i_1 + i_2$  is higher ( $1.9 \times 10^{-15} \text{ A}/\text{cm}^2$ ) as compared to passivated samples that underwent the HPT both

at 13.56 and 40.68 MHz frequencies. This shows higher interfacial and bulk defects (unsatisfactory bonds) for  $i_1 + i_2$  passivated samples. The application of VHF-HPT facilitates the microstructure of the a-Si layer for better c-Si surface passivation with reduced density of defect states at the c-Si/a-Si interface. To further understand better the generated plasma with different experimental conditions for the i-layer deposition, in situ optical emission spectroscopy (OES) is used.

Figure 4 shows the optical emission line intensities in the range of 200–800 nm of various excited molecules/atoms ( $\text{Si}^*$ ,  $\text{SiH}^*$ ,  $\text{H}\alpha$ ) with different recipes like pure  $\text{SiH}_4$ ,  $\text{SiH}_4:\text{H}_2$ , in a ratio of 1:5, and HPT at different frequencies. The  $\text{Si}^*$  and  $\text{SiH}^*$  emission lines are observed from pure  $\text{SiH}_4$  of 40 sccm (Figure 4a), whereas with the  $\text{SiH}_4:\text{H}_2$  of 20:100 sccm additional  $\text{H}\alpha$  peak is also observed (Figure 4b). The main observation from Figure 4c,d shows different  $\text{H}\alpha$  line intensities with RF-HPT and VHF-HPT for the same gas flow and power densities. During the HPT post-treatment process, the hydrogen species diffuses through the a-Si matrix, replacing the weak Si–Si bond with the more stable Si–H bonds, thus improving the passivation.<sup>32</sup> Whereas in the case of VHF-HPT treatment, due to the reduction of plasma sheath thickness near the electrode, it can reduce high-energy ion bombardment as fewer excited hydrogen radicals reach the stack of the  $i_1 + i_2$  layer. As there are large neutral hydrogen radicals, their coverage increases on the growing film surface.<sup>33</sup> Consequently, these radicals have a higher chance of reaching energetically favorable sites, forming a highly ordered silicon network. This process can aid in the onset of the film transition zone, further remarkably improving the passivation using VHF-HPT treatment.<sup>34</sup>

The hydrogen ion bombardment energy ranges from 5–20 eV, as shown by Kondo and Smets et al., demonstrating that ion bombardment energy considerably affects the crystallinity,<sup>35,36</sup> hence, in VHF-HPT, lesser damage is expected due to the reduction of ion energy. However, in the case of RF-HPT, it causes bombardment of high energy ions<sup>13</sup> as evident from higher  $\text{H}\alpha$  intensity, which probably causes higher etching and disrupted bonding in the  $i_2$  layer, hence a less effective lifetime value obtained. Different frequencies of the excitation source (13.56 MHz and VHF 40.68 MHz) modify the energy distribution shape of hydrogen ions/radicals, which in turn affects the energy dispersion in the plasma.<sup>13</sup> Thus, using a higher frequency of 40.68 MHz for HPT can produce a better microstructure of film, giving desirable c-Si surface passivation.<sup>19</sup>

Figure 5 shows the spectra of the imaginary part of the pseudo dielectric function  $\langle \epsilon_2 \rangle$  and film thickness of the i-a-Si:H layer deposited on a polished silicon wafer with different conditions. The combination of  $i_1$ - and  $i_2$ -a-Si:H films showed a higher amplitude of  $\langle \epsilon_2 \rangle$ , representing a relatively lower void fraction of ~25.3%, which is estimated using Bruggeman effective medium approximation. The formation of the dense film is due to H diffusion from the  $i_2$  (hydrogen diluted) a-Si:H layer to the porous  $i_1$ -a-Si:H layer. With the RF-HPT, the spectrum amplitude reduced with onset from the relatively lower energy, and the estimated void fraction increased to ~34.5%, indicating an abrupt change in the microstructure of the amorphous network (Si–H and Si–H<sub>2</sub> bonding environment). Whereas with the VHF-HPT, it is found to have fewer changes in the microstructure of the amorphous network as the amplitude of the  $\epsilon_2$  reduced slightly with the estimated void

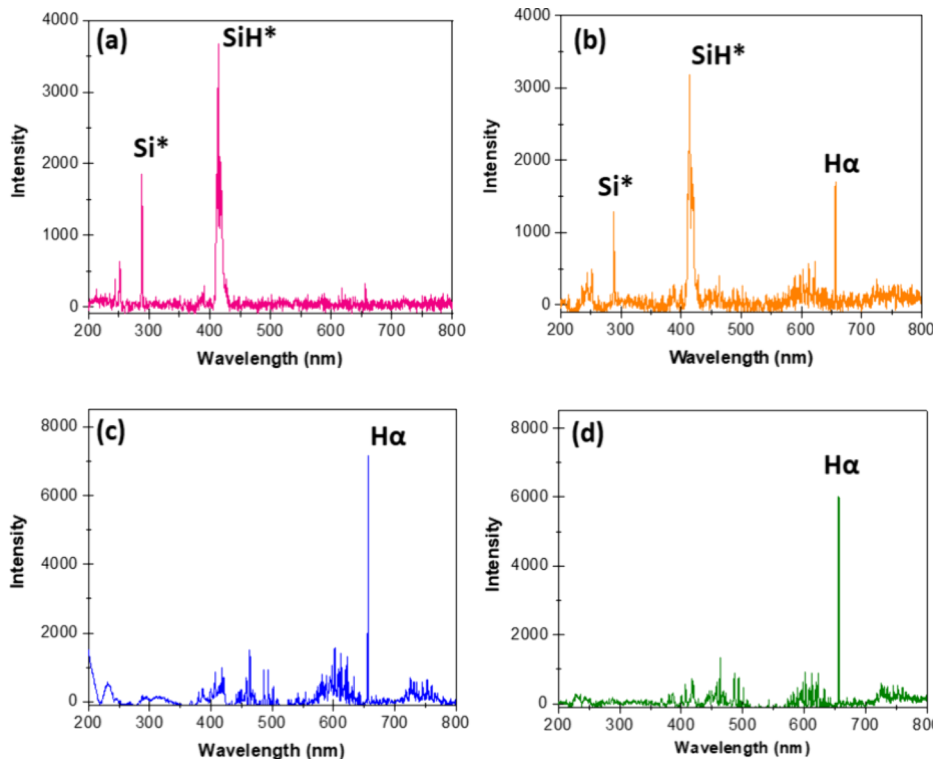


**Figure 4.** Optical emission spectra recorded from the generated plasma in a reaction chamber for (a)  $i_1$ , pure silane 40 sccm at 50 Pa (b)  $i_2$ ,  $\text{SiH}_4/\text{H}_2$ : 20/100 sccm at 80 Pa (c) RF-HPT @ 250 sccm  $\text{H}_2$  at 133 Pa (d) VHF-HPT @ 250 sccm  $\text{H}_2$  at 133 Pa.

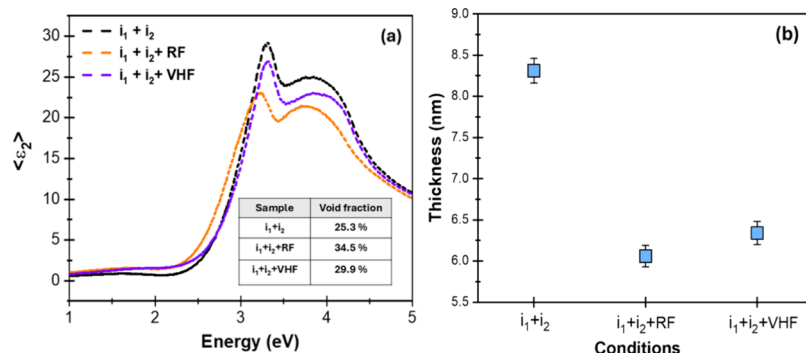


**Figure 5.** (a) Imaginary part of the pseudo dielectric function  $\langle \epsilon_2 \rangle$  spectra, and (b) thickness variation of i-a-Si:H layers deposited on a polished silicon wafer with different conditions after correction with a geometrical factor of 1.73.

fraction of  $\sim 29.9\%$ . The thickness of the i-a-Si:H bilayer stack has reduced from  $\sim 8.31$  to  $\sim 6.06$  nm with the RF-HPT (Figure 5b); this shows the strong etching effect due to hydrogen ion/radical bombardment creating many voids. Meanwhile, the film thickness is  $\sim 6.34$  nm for the VHF-HPT, indicating a reduced etching effect from the hydrogen ion concentration supported by the OES analysis (Figure 4). The thin, positively charged region near the anode surface acts like a capacitor with lower impedance at higher frequencies, resulting in many low-energy ions.<sup>18</sup> These ions cause more hydrogen infusion into the stack but with less etching effect, resulting in thicker intrinsic films with better hydrogenation and defects passivation.

As illustrated in Figure 6a, significant degradation in the MCL is observed across the carrier injection range following ITO deposition on both sides of the device structure. The structure consists of p-a-Si:H/i-a-Si:H/n-c-Si/i-a-Si:H/nc-n-Si:H; here  $i_1 + i_2 + \text{VHF}$  is the passivation layer on both sides.

At a carrier injection level of  $1 \times 10^{15} \text{ cm}^{-3}$ , the MCL decreases from 2.7 to 1.35 ms. The sputtering damage arises from luminescence produced by oxygen and argon plasma, as well as high-energy ion bombardment impacting the films during the ITO deposition process.<sup>37</sup> Such interactions can lead to the formation of metastable defects within the bulk of the amorphous silicon (a-Si:H) layer or on the c-Si wafer surface. Additionally, secondary electron emission and energy during ion neutralization can result in the excitation of excess charge carriers within the a-Si:H film. This process may lead to the release of hydrogen and the disruption of Si–H bonds in the a-Si:H film or the c-Si surface, further weakening surface passivation.<sup>38</sup> It is reported that this damage can be recovered by annealing,<sup>39</sup> but our structures have shown irreversible degradation. Therefore, time-of-flight secondary ion mass spectrometry (TOF-SIMS) was adopted to determine the effect of ITO deposition at the interfaces for identifying the species present. Figure 6b shows that  $\text{In}^+$  and  $\text{O}^+$  ions

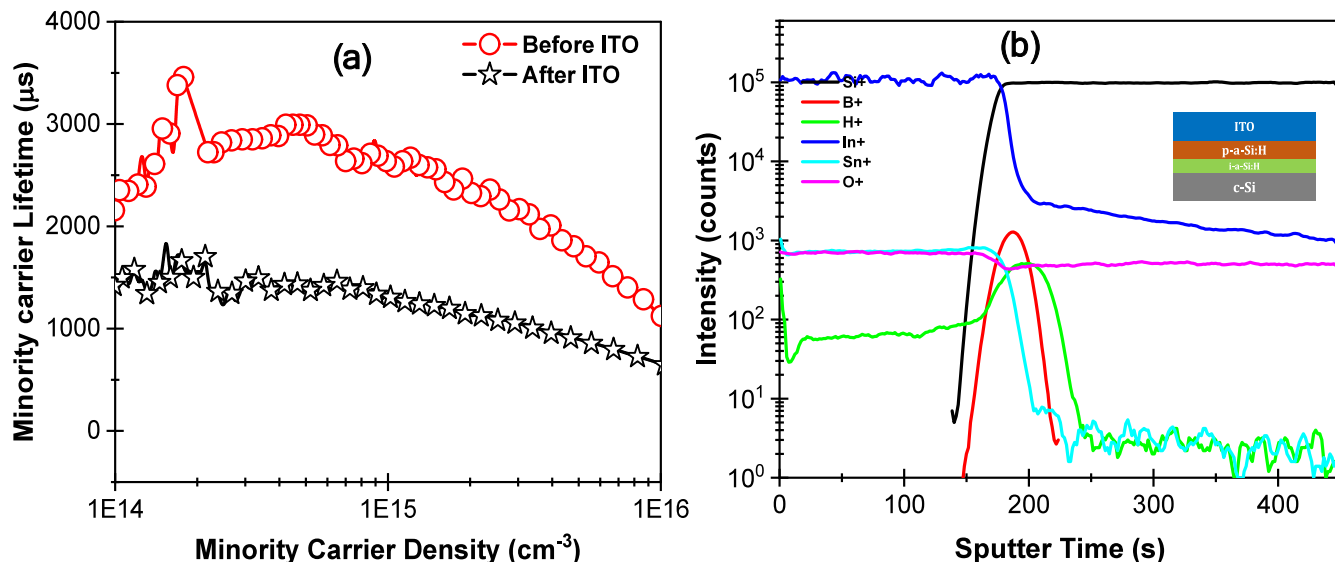


**Figure 6.** (a) Carrier injection-dependent lifetime graphs of the SHJ structure with an  $i_1 + i_2 + \text{VHF}$  passivation layer followed by cell precursors and after ITO deposition, (b) SIMS profile of the test structure of ITO/p-a-Si:H/i-a-Si:H/c-Si on polished c-Si wafer.

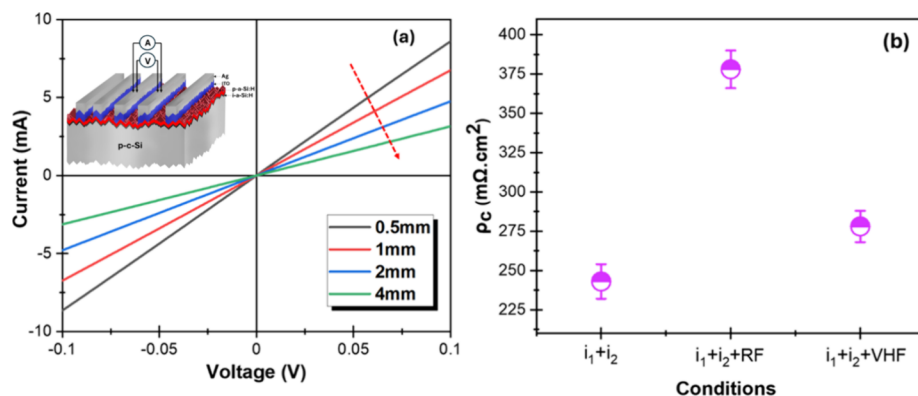


**Figure 7.** (a) Schematic of test structure and current vs voltage plot of TLM resistance measurements of  $i_1 + i_2 + \text{VHF}$  condition. (b) Extracted contact resistivities using the p-c-Si/i-a-Si:H/p-a-Si:H/TCO/Ag test structure with different i-layer conditions.

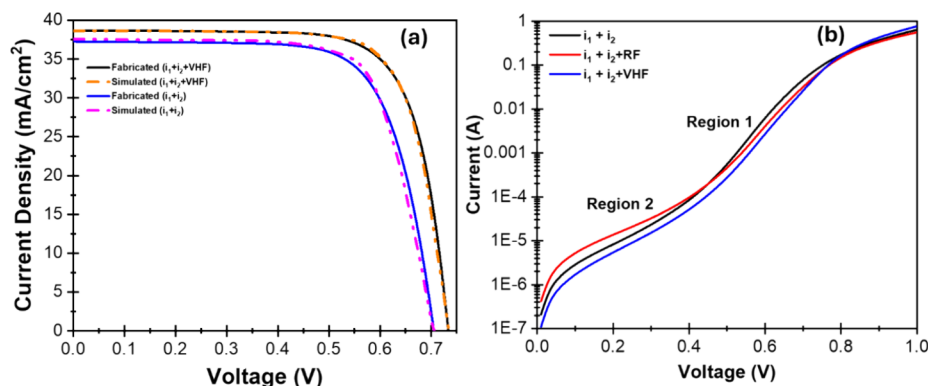


**Figure 8.** (a) Fabricated SHJ cells J-V graphs under light conditions along with simulated (3D) J-V graphs with and without VHF-HPT treated i-layer stack, and (b) semilog I-V graphs under dark conditions with different i-layer conditions.

penetrated the bulk of the c-Si wafer through the i- and p-a-Si:H layers during ITO deposition; a similar effect was observed in the stack of i-a-Si:H and nc-n-Si:H layers. This penetration of these ions could lead to additional doping or counter-doping and structural defects, complicating the films and interface properties, which might create shunting paths with the unwanted recombination current ( $J_0$ ) in a device.

Thus, optimizing the ITO deposition is essential for producing high-efficiency solar cells with minimal sputter damage during deposition.

The TLM measurements were also performed to understand the i-layer role in hole-selective contact resistance based on the modification for integration into an SHJ device by depositing coplanar electrodes. The electrode with a length of 15 mm and

a width of 1 mm, on the layers under study, deposited on p-type c-Si textured wafers having distances of 0.5, 1, 2, and 4 mm using a shadow mask as seen in Figure 7a. Using the I–V characteristics, the contact resistivities ( $\rho_c$ ) are calculated, Figure 7b illustrates the impact of different i-a-Si:H layers on  $\rho_c$ . With the  $i_1 + i_2$  layer, we have observed a  $\rho_c$  of  $\sim 250$  m $\Omega$ -cm $^2$ ; with the  $i_1 + i_2 +$  RF-HPT structure, the  $\rho_c$  value enhanced to  $\sim 378$  m $\Omega$ -cm $^2$ . This increase is attributed to an enhancement in the void fraction percentage (illustrated in Figure 5a) within the film, which impacts carrier transport. On the other hand, the VHF-HPT demonstrates a reduction in the  $\rho_c$  to  $\sim 278$  m $\Omega$ -cm $^2$  when compared to RF-HPT, which is slightly higher than the  $i_1 + i_2$  structure. Therefore, the VHF-HPT treatment achieves a better balance between passivation (Figure 2) and carrier transport (reflected in the lower  $\rho_c$  with an optimal void fraction) for the efficient trap-assisted tunneling (TAT) process. The effects of the i-layer stack exposed to RF-HPT and VHF-HPT treatment have been further examined in relation to the device operation.

Figure 8 displays the light J-V along with simulated (3D) J-V and dark I–V graphs of SHJ cells under various i-layer conditions, and Table 2 shows the light J-V parameters of the

**Table 2. Light J-V Parameters of Fabricated SHJ Cell with Different Passivating i-Layers**

sample ID	$V_{oc}$ (mV)	$J_{sc}$ (mA/cm $^2$ )	FF (%)	$\eta$ (%)	$R_s$ ( $\Omega$ -cm $^2$ )
$i_1 + i_2$	705	37.24	71.64	18.81	1.27
$i_1 + i_2 +$ RF	721	38.13	72.79	20.01	1.25
$i_1 + i_2 +$ VHF	733	38.67	75.20	21.31	1.08

front emitter SHJ device fabricated with different i-layer conditions. The combination of the  $i_1$  and  $i_2$  layers resulted in a  $V_{oc}$  of  $\sim 705$  mV, which increased to about  $\sim 721$  mV following RF-HPT. The most notable enhancement occurred with the VHF-HPT treatment, yielding a  $V_{oc}$  of  $\sim 733$  mV. With the HPTs treatment, the dark I–V graph shows (Figure 8b) a shift toward higher voltage and lower current, reflecting improved junction characteristics. Furthermore, the diode characteristics reveal double diode transport mechanisms across two distinct voltage ranges: region 1 (0.5 to 0.75 V) and region 2 (0.15 to 0.4 V). The diode quality factor ( $n$ ) and reverse saturation current ( $J_0$ ) are determined from the slope and intercept of the J-V graphs in these regions, as well as estimated through curve fitting using a double diode model by nanohub software.<sup>40</sup>

Table 3 shows diode parameters extracted from the dark J-V graphs of the SHJ cells with different i-layer conditions. The i layers influence both parameters  $n$  and  $J_0$ , as these layers modify the recombination rates and introduce additional resistance at the interface. It is essential to consider both factors collectively to evaluate the device's performance.<sup>41</sup> Nevertheless, a reduction in  $J_0$  is preferable for enhancing the device's performance. The  $J_{01}$  is the lowest for the VHF-HPT

case, indicating minimal recombination in the emitter and rear junction regions, and lower  $J_{02}$  ( $\sim 1 \times 10^{-7}$  A/cm $^2$ ) represents reduced recombination in the space charge region of the cell junction. The RF-HPT-treated i-layer shows the highest  $J_{01}$  ( $\sim 1.24 \times 10^{-10}$  A/cm $^2$ ) and  $J_{02}$  ( $\sim 6.1 \times 10^{-7}$  A/cm $^2$ ) and  $n_1$  (1.45) and  $n_2$  (4.1) because a higher void fraction of  $\sim 34.5\%$  is observed for this sample. These voids introduce additional recombination centers and leakage paths in a device. Also, these voids may make layers more prone to sputter damage, limiting the device's performance despite having better passivation with the HPT.

Figure 9 shows the light J-V, dark J-V, Suns- $V_{oc}$ , and simulated J-V graphs (using nanohub software) of the  $i_1 + i_2 +$

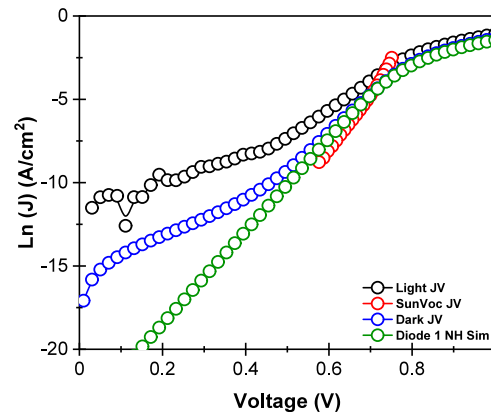


**Figure 9.** Suns- $V_{oc}$ , Dark J-V, and short-circuit current-adjusted light J-V graphs of the cell with the passivating  $i_1 + i_2 +$  VHF stack along with the simulated J-V graph using nanohub software.

VHF passivated SHJ cell. The light J-V graph was plotted after adjusting the current by adding the short-circuit current density. The Sun- $V_{oc}$  curve has measured intensity values down to 0.01 sun only, resulting in a lack of data below  $\sim 0.6$  V. Consequently, it was not possible to compare the parameters for diode 2 at lower voltages for Suns- $V_{oc}$ , while measurements for dark and light J-V were collected across the entire voltage range. The following equation typically describes the dark characteristics by a double diode model in the medium and higher voltage range.

$$J = J_{01} \exp \frac{q(V + JR_S)}{n_1 KT} + J_{02} \exp \frac{q(V + JR_S)}{n_2 KT} + \frac{V + JR_S}{R_{sh}}$$

Where  $V$  and  $J$  are the voltage and current density,  $R_s$  and  $R_{sh}$  are the series and shunt resistances of the device, and  $n_1/n_2$  and  $J_{01}/J_{02}$  are the diode quality factor and reverse saturation current density of diode 1/diode 2. The analysis revealed that the values of  $n_1$  and  $J_{01}$  were consistently higher in both dark and light J-V characteristics compared to the values from the Suns- $V_{oc}$  graph as shown in Table 4.

**Table 3. Diode Parameters Extracted from Dark I–V Graphs by Fitting the Double Diode Model**

sample ID	parameters in region 1		parameters in region 2			
	diode quality factor ( $n_1$ )	reverse saturation current ( $J_{01}$ ) (A·cm $^{-2}$ )	diode quality factor ( $n_2$ )	reverse saturation current ( $J_{02}$ ) (A·cm $^{-2}$ )	shunt resistance ( $\Omega$ ·cm $^{-2}$ )	series resistance ( $\Omega$ ·cm $^{-2}$ )
$i_1 + i_2$	1.39	$7.80 \times 10^{-11}$	3.5	$2.7 \times 10^{-7}$	$2.40 \times 10^5$	1.39
$i_1 + i_2 +$ RF	1.45	$1.24 \times 10^{-10}$	4.1	$6.1 \times 10^{-7}$	$1.25 \times 10^5$	1.25
$i_1 + i_2 +$ VHF	1.40	$3.64 \times 10^{-11}$	3.3	$1.0 \times 10^{-7}$	$3.20 \times 10^5$	0.80

**Table 4.** SHJ Cell Parameters with the  $i_1 + i_2 + \text{VHF}$  Passivated Layers Extracted from Light, Suns- $V_{oc}$ , and Dark J-V Graphs

graphs	$n_1$	$J_{01}$ (A/cm <sup>2</sup> )	$n_2$	$J_{02}$ (A/cm <sup>2</sup> )
Suns- $V_{oc}$	1.19	$1.1 \times 10^{-12}$		
Dark Fit	1.40	$3.64 \times 10^{-11}$	3.3	$1.00 \times 10^{-7}$
Light Fit	2.04	$1.40 \times 10^{-7}$	5.2	$1.24 \times 10^{-5}$

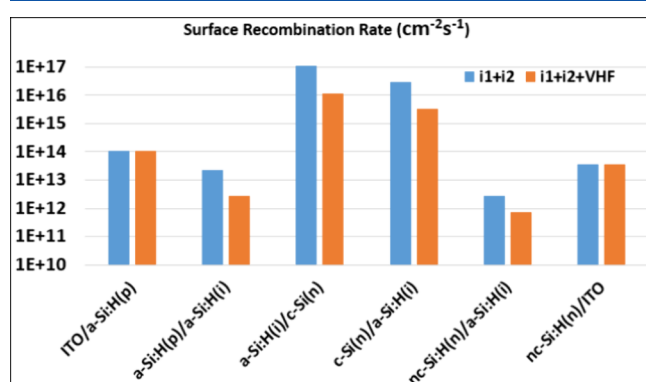
The Suns- $V_{oc}$  (series resistance free) parameters for the  $n_1$  diode are derived within the same voltage range as the dark and light J-V graphs. The  $n_1$  and  $J_{01}$  illustrated for light and dark J-V are obtained from the voltage region close to the open-circuit voltage. This observation highlights a notable decline in performance parameters due to recombination within the cell's operating range of 0.5 to 0.7 V. The observed discrepancy in this region accounts for the significant impact of elevated series resistance ( $R_s$ ) and elevated recombination when exposed to light. The good fit between the simulated and experimental dark J-V graphs validates the model and the extracted parameters. Table 4 illustrates that with an optimized i-layer, SHJ cells excel in minimizing recombination losses under ideal conditions, as seen in the Suns- $V_{oc}$  graph, but the presence of defects and trap centers at lower injection leads to significant recombination under both dark and illuminated conditions, as indicated by the higher  $J_0$  values. For Suns- $V_{oc}$ , the  $J_{01}$  value is much lower ( $1.1 \times 10^{-12}$  A/cm<sup>2</sup>) than the value obtained for dark and light J-V graphs, which is characteristic of high passivation quality SHJ solar cells with the VHF-HPT. In dark conditions, the  $J_{01}$  value rises to  $3.64 \times 10^{-11}$  A/cm<sup>2</sup>, and at lower voltages, a  $J_{02}$  value of  $1 \times 10^{-7}$  A/cm<sup>2</sup> appears. This increase indicates that recombination becomes more significant in the dark, likely due to trap-assisted recombination at the interfaces. The higher value of  $J_{02}$  suggests that recombination pathways or leaky diodes are present at the heterojunction interface under dark conditions, which become more prominent under light, resulting in higher saturation current and ideality factor under light compared to dark conditions. Under light at higher voltages, where  $J_{01}$  and  $n_1$  are determined, an increase or deviation may be attributed to series resistance in the cell, which can affect the  $J_{01}$  ( $1.47 \times 10^{-7}$  A/cm<sup>2</sup>), restricting current flow, and cause a voltage drop. At lower voltages, below the built-in voltage under illumination, the injected electron-hole pairs find enough interface defects to produce recombination current, leading to higher  $J_{02}$  ( $1.24 \times 10^{-5}$  A/cm<sup>2</sup>) and the deviation of the ideality factor  $n_2$  (5.2) from its dark value of 3.3.

The (3D) numerically simulated J-V graphs of SHJ cells without and with VHF-HPT using TCAD are presented in Figure 8, which are matched with the fabricated J-V characteristics by varying the i-a-Si:H bulk and c-Si/i-a-Si:H interface defect densities by keeping other electronic/optical parameters the same (provided in the Supporting Information). Some of the parameters of SHJ cells and defect distribution are adopted from the literature.<sup>42,43</sup> The considered defect details and capture cross sections are shown in Table 5. The capture cross sections and energy positions of defects are kept intact; only the concentrations of defects are varied for different conditions. The thickness and energy bandgap variation of i-layers are considered according to our experimental observations. From Table 5, one can infer that the i-a-Si:H bulk defects dominate the device performance, which the VHF-HPT strongly suppresses. From the

**Table 5.** Considered Defects in the Bulk i-a-Si:H and i-a-Si:H/c-Si Interface

	a-Si:H(i)/c-Si(n)	bulk i-layer	bulk i-layer
	eXection = hXection = $10^{-14}$ cm <sup>2</sup>	Gaussian dangling bond	exponential tail states
$i_1 + i_2$	$1 \times 10^{11}$ cm <sup>-2</sup>	$1 \times 10^{18}$ cm <sup>-3</sup>	$1 \times 10^{20}$ cm <sup>-3</sup>
$i_1 + i_2 + \text{VHF}$	$5 \times 10^{10}$ cm <sup>-2</sup>	$1 \times 10^{16}$ cm <sup>-3</sup>	$1 \times 10^{18}$ cm <sup>-3</sup>

obtained simulation data, surface recombination rates are also plotted without and with VHF-HPT. From Figure 10, one can

**Figure 10.** Surface recombination rates at different interfaces of cells with  $i_1 + i_2$  and  $i_1 + i_2 + \text{VHF}$  passivation layers.

observe that with the VHF-HPT, charge carrier recombination at the c-Si(n)/a-Si:H(i), a-Si:H(p)/a-Si:H(I), and nc-Si:H(n)/a-Si:H(i) interfaces is reduced. Hence, simulation in TCAD well supports the improvement by the VHF-HPT treatment and the observed experimental results related to hydrogenation of the bulk i-a-Si:H layer as well as the c-Si(n)/i-a-Si:H interface.

#### 4. CONCLUSIONS

We have observed the VHF-HPT effect on the i-layer stack with an enhancement in the MCL from 1.2 to 2.7 ms from the symmetrically passivated c-Si wafer due to better hydrogenation of the i-a-Si:H bulk and c-Si/i-a-Si:H interface compared to without treatment. Observed film density and thickness variation through ellipsometry analysis is supported by the in situ optical emission study, where the generated hydrogen ion/radical played a key role in compact film formation and thickness reduction. This phenomenon is also verified through contact resistance measurements, where we have observed contact resistivity of  $\sim 278$  mΩ·cm<sup>2</sup> from the hole-selective stack compared to RF-HPT treatment having  $\sim 378$  mΩ·cm<sup>2</sup>. The treated i-layers are also integrated into the SHJ device structure, and we observed an overall device performance enhancement to  $\sim 21\%$  from  $\sim 19\%$ , with significant improvement in  $V_{oc}$  from  $\sim 707$  to  $\sim 733$  mV. We further observed from J-V graphs of the SHJ cell obtained through Suns- $V_{oc}$  that dark and light have carrier recombination dominance despite the VHF-HPT. Numerical simulations have also shown a few orders of reduction in recombination in the bulk i-a-Si:H and c-Si/i-a-Si:H interface defect states when the bilayer stack is treated with the VHF-HPT.

## ASSOCIATED CONTENT

### Supporting Information

The Supporting Information is available free of charge at <https://pubs.acs.org/doi/10.1021/acsaem.4c02475>.

Details of TCAD simulation, simulation method, and physical parameters ([PDF](#))

## AUTHOR INFORMATION

### Corresponding Author

Vamsi Krishna Komarala – Solar Photovoltaics Laboratory,  
Department of Energy Science and Engineering, Indian  
Institute of Technology Delhi, New Delhi 110 016, India;  
Email: [vamsi@iitd.ac.in](mailto:vamsi@iitd.ac.in)

### Authors

Ashutosh Pandey – Solar Photovoltaics Laboratory,  
Department of Energy Science and Engineering, Indian  
Institute of Technology Delhi, New Delhi 110 016, India;  
[orcid.org/0000-0002-5582-7406](https://orcid.org/0000-0002-5582-7406)

Shrestha Bhattacharya – Solar Photovoltaics Laboratory,  
Department of Energy Science and Engineering, Indian  
Institute of Technology Delhi, New Delhi 110 016, India;  
[orcid.org/0009-0007-2122-0271](https://orcid.org/0009-0007-2122-0271)

Shahnawaz Alam – Solar Photovoltaics Laboratory,  
Department of Energy Science and Engineering, Indian  
Institute of Technology Delhi, New Delhi 110 016, India

Silajit Manna – Solar Photovoltaics Laboratory, Department  
of Energy Science and Engineering, Indian Institute of  
Technology Delhi, New Delhi 110 016, India

Sourav Sadhukhan – Solar Photovoltaics Laboratory,  
Department of Energy Science and Engineering, Indian  
Institute of Technology Delhi, New Delhi 110 016, India

Son Pal Singh – Solar Photovoltaics Laboratory, Department  
of Energy Science and Engineering, Indian Institute of  
Technology Delhi, New Delhi 110 016, India

Complete contact information is available at:

<https://pubs.acs.org/10.1021/acsaem.4c02475>

### Notes

The authors declare no competing financial interest.

## ACKNOWLEDGMENTS

The authors would like to acknowledge the financial support from the Department of Science and Technology (DST), Government of India, under the Solar Challenge Award; grant number DST/ETC/CASE/RES/2023/04G, under the Water and Clean Energy area; grant number DST/TMD/CERI/RES/2020/48G, under the Nano Mission; grant number DST/NM/NT/2023/03(G)/1 of the Technology Mission Division. The authors also want to acknowledge the Nanoscale Research Facility (NRF) of IIT Delhi for the clean room facility to fabricate SHJ solar cells and the Central Research Facility (CRF) for sample characterization.

## REFERENCES

- (1) Mishima, T.; Taguchi, M.; Sakata, H.; Maruyama, E. Development Status of High-Efficiency HIT Solar Cells. *Sol. Energy Mater. Sol. Cells* **2011**, *95* (1), 18–21.
- (2) Liu, W.; Liu, Y.; Yang, Z.; Xu, C.; Li, X.; Huang, S.; Shi, J.; Du, J.; Han, A.; Yang, Y.; Xu, G.; Yu, J.; Ling, J.; Peng, J.; Yu, L.; Ding, B.; Gao, Y.; Jiang, K.; Li, Z.; Yang, Y.; Li, Z.; Lan, S.; Fu, H.; Fan, B.; Fu, Y.; He, W.; Li, F.; Song, X.; Zhou, Y.; Shi, Q.; Wang, G.; Guo, L.; Kang, J.; Yang, X.; Li, D.; Wang, Z.; Li, J.; Thoroddson, S.; Cai, R.; Wei, F.; Xing, G.; Xie, Y.; Liu, X.; Zhang, L.; Meng, F.; Di, Z.; Liu, Z. Flexible Solar Cells Based on Foldable Silicon Wafers with Blunted Edges. *Nature* **2023**, *617* (7962), 717–723.
- (3) Pomaska, M.; Köhler, F.; Zastrow, U.; Mock, J.; Pennartz, F.; Muthmann, S.; Astakhov, O.; Carius, R.; Finger, F.; Ding, K. New Insight into the Microstructure and Doping of Unintentionally N-Type Microcrystalline Silicon Carbide. *J. Appl. Phys.* **2016**, *119* (17), 175303.
- (4) Singh, K.; Nayak, M.; Singh, S.; Komarala, V. K. Investigation of Silicon Surface Passivation by Sputtered Amorphous Silicon and Thermally Evaporated Molybdenum Oxide Films Using Temperature- and Injection-Dependent Lifetime Spectroscopy. *Semicond. Sci. Technol.* **2020**, *35* (12), 125017.
- (5) Olibet, S.; Vallat-Sauvain, E.; Ballif, C. Model for A-Si:H/c-Si Interface Recombination Based on the Amphoteric Nature of Silicon Dangling Bonds. *Phys. Rev. B - Condens. Matter Mater. Phys.* **2007**, *76* (3), No. 035326.
- (6) Froitzheim, A.; Brendel, K.; Elstner, L.; Fuhs, W.; Kliefeth, K.; Schmidt, M. Interface Recombination in Heterojunctions of Amorphous and Crystalline Silicon. *J. Non. Cryst. Solids* **2002**, *299*–302 (PART 1), 663–667.
- (7) Descoedres, A.; Barraud, L.; De Wolf, S.; Strahm, B.; Lachenal, D.; Guérin, C.; Holman, Z. C.; Zicarelli, F.; Demaurex, B.; Seif, J.; Holovsky, J.; Ballif, C. Improved Amorphous/Crystalline Silicon Interface Passivation by Hydrogen Plasma Treatment. *Appl. Phys. Lett.* **2011**, *99* (12), 123506.
- (8) Jik Lee, S.; Hwan Kim, S.; Won Kim, D.; Hyung Kim, K.; Kyu Kim, B.; Jang, J. Effect of Hydrogen Plasma Passivation on Performance of HIT Solar Cells. *Sol. Energy Mater. Sol. Cells* **2011**, *95* (1), 81–83.
- (9) Zhang, Q.; Zhu, M.; Liu, F.; Zhou, Y. The Optimization of Interfacial Properties of Nc-Si:H/c-Si Solar Cells in Hot-Wire Chemical Vapor Deposition Process. *J. Mater. Sci. Mater. Electron.* **2007**, *18* (S1), 33–36.
- (10) Mews, M.; Schulze, T. F.; Mingirulli, N.; Korte, L. Hydrogen Plasma Treatments for Passivation of Amorphous-Crystalline Silicon-Heterojunctions on Surfaces Promoting Epitaxy. *Appl. Phys. Lett.* **2013**, *102* (12), 122106.
- (11) Liu, W.; Zhang, L.; Cong, S.; Chen, R.; Wu, Z.; Meng, F.; Shi, Q.; Liu, Z. Controllable A-Si:H/c-Si Interface Passivation by Residual SiH<sub>4</sub> Molecules in H<sub>2</sub> Plasma. *Sol. Energy Mater. Sol. Cells* **2018**, *174*, 233–239.
- (12) Morales-Vilches, A. B.; Wang, E. C.; Henschel, T.; Kubicki, M.; Cruz, A.; Janke, S.; Korte, L.; Schlatmann, R.; Stannowski, B. Improved Surface Passivation by Wet Texturing, Ozone-Based Cleaning, and Plasma-Enhanced Chemical Vapor Deposition Processes for High-Efficiency Silicon Heterojunction Solar Cells. *Phys. Status Solidi Appl. Mater. Sci.* **2020**, *217* (4), No. 1900518.
- (13) Sai, H.; Chen, P.-W.; Hsu, H.-J.; Matsui, T.; Nunomura, S.; Matsubara, K. Impact of Intrinsic Amorphous Silicon Bilayers in Silicon Heterojunction Solar Cells. *J. Appl. Phys.* **2018**, *124* (10), 103102.
- (14) De Wolf, S.; Fujiwara, H.; Kondo, M. Impact of Annealing on Passivation of A-Si:H/c-Si Heterostructures. In *2008 33rd IEEE Photovoltaic Specialists Conference*; IEEE, 2008; 1–4.
- (15) Duan, W.; Lambertz, A.; Bittkau, K.; Qiu, D.; Qiu, K.; Rau, U.; Ding, K. A Route towards High-efficiency Silicon Heterojunction Solar Cells. *Prog. Photovoltaics Res. Appl.* **2022**, *30* (4), 384–392.
- (16) Curtins, H.; Wyrsch, N.; Favre, M.; Shah, A. V. Influence of Plasma Excitation Frequency Fora-Si:H Thin Film Deposition. *Plasma Chem. Plasma Process.* **1987**, *7* (3), 267–273.
- (17) Zhao, Y.; Mazzarella, L.; Procel, P.; Han, C.; Yang, G.; Weeber, A.; Zeman, M.; Isabella, O. Doped Hydrogenated Nanocrystalline Silicon Oxide Layers for High-efficiency C-Si Heterojunction Solar Cells. *Prog. Photovoltaics Res. Appl.* **2020**, *28* (5), 425–435.
- (18) Schwarzenbach, W.; Howling, A. A.; Fivaz, M.; Brunner, S.; Hollenstein, C. Sheath Impedance Effects in Very High Frequency

- Plasma Experiments. *J. Vac. Sci. Technol. A Vacuum, Surfaces, Film.* **1996**, *14* (1), 132–138.
- (19) Sharma, S.; Sirse, N.; Kuley, A.; Turner, M. M. Ion Energy Distribution Function in Very High Frequency Capacitive Discharges Excited by Saw-Tooth Waveform. *Phys. Plasmas* **2021**, *28* (10), 103502.
- (20) Khanna, A.; Mueller, T.; Stangl, R. A.; Hoex, B.; Basu, P. K.; Aberle, A. G. A Fill Factor Loss Analysis Method for Silicon Wafer Solar Cells. *IEEE J. Photovoltaics* **2013**, *3* (4), 1170–1177.
- (21) McIntosh, K. R.; Black, L. E. On Effective Surface Recombination Parameters. *J. Appl. Phys.* **2014**, *116* (1), No. 014503.
- (22) Wolf, M.; Rauschenbach, H. Series Resistance Effects on Solar Cell Measurements. *Adv. Energy Convers.* **1963**, *3* (2), 455–479.
- (23) Shockley, W.; Read, W. T. Statistics of the Recombinations of Holes and Electrons. *Phys. Rev.* **1952**, *87* (5), 835–842.
- (24) Bhattacharya, S.; Pandey, A.; Alam, S.; Komarala, V. K. Development of High Conducting Phosphorous Doped Nanocrystalline Thin Silicon Films for Silicon Heterojunction Solar Cells Application. *Nanotechnology* **2024**, *35* (32), 325701.
- (25) Pandey, A.; Bhattacharya, S.; Panigrahi, J.; Mandal, S.; Komarala, V. K. Investigation of Dual Intrinsic A-Si:H Films for Crystalline Silicon Surface Passivation by Spectroscopic Ellipsometry: Application in Silicon Heterojunction Solar Cells. *Appl. Phys. A: Mater. Sci. Process.* **2023**, *129* (8), 575.
- (26) Alam, S.; Pandey, A.; Bhattacharya, S.; Mandal, S.; Komarala, V. K. Investigation of Optoelectronic Properties of Tin-Doped Indium Oxide Thin Films and Contact Resistivity with Silver Film: Role of Oxygen Concentration Variation during Sputter Deposition. *Thin Solid Films* **2024**, *799*, No. 140398.
- (27) McIntosh, K. R.; Johnson, L. P. Recombination at Textured Silicon Surfaces Passivated with Silicon Dioxide. *J. Appl. Phys.* **2009**, *105* (12), 124520.
- (28) Serenelli, L.; Chierchia, R.; Izzi, M.; Tucci, M.; Martini, L.; Caputo, D.; Asquini, R.; De Cesare, G. Hydrogen Plasma and Thermal Annealing Treatments on A-Si:H Thin Film for c-Si Surface Passivation. *Energy Procedia* **2014**, *60* (C), 102–108.
- (29) Cuevas, A. The Recombination Parameter  $J_0$ . *Energy Procedia* **2014**, *55*, 53–62.
- (30) Janssen, G. J. M.; Wu, Y.; Tool, K. C. J. J.; Romijn, I. G.; Fell, A. Extraction of Recombination Properties from Lifetime Data. *Energy Procedia* **2016**, *92*, 88–95.
- (31) Black, L. E.; Kho, T. C.; McIntosh, K. R.; Cuevas, A. The Influence of Orientation and Morphology on the Passivation of Crystalline Silicon Surfaces by Al<sub>2</sub>O<sub>3</sub>. *Energy Procedia* **2014**, *55*, 750–756.
- (32) Lee, S.; Park, J.; Pham, D. P.; Kim, S.; Kim, Y.; Trinh, T. T.; Dao, V. A.; Yi, J. The Impact of the Micro-Structure within Passivated Layers on the Performance of the a-Si:H/c-Si Heterojunction Solar Cells. *Energies* **2023**, *16* (18), 6694.
- (33) Liu, W.; Zhang, L.; Chen, R.; Meng, F.; Guo, W.; Bao, J.; Liu, Z. Underdense A-Si:H Film Capped by a Dense Film as the Passivation Layer of a Silicon Heterojunction Solar Cell. *J. Appl. Phys.* **2016**, *120* (17), 175301.
- (34) Ge, J.; Ling, Z. P.; Wong, J.; Stangl, R.; Aberle, A. G.; Mueller, T. Analysis of Intrinsic Hydrogenated Amorphous Silicon Passivation Layer Growth for Use in Heterojunction Silicon Wafer Solar Cells by Optical Emission Spectroscopy. *J. Appl. Phys.* **2013**, *113* (23), 234310.
- (35) Smets, A. H. M.; Kondo, M. The Role of Ion-Bulk Interactions during High Rate Deposition of Microcrystalline Silicon by Means of the Multi-Hole-Cathode VHF Plasma. *J. Non. Cryst. Solids* **2006**, *352* (9–20), 937–940.
- (36) Kondo, M. Microcrystalline Materials and Cells Deposited by RF Glow Discharge. *Sol. Energy Mater. Sol. Cells* **2003**, *78* (1–4), 543–566.
- (37) Demaurex, B.; De Wolf, S.; Descoeuilles, A.; Charles Holman, Z.; Ballif, C. Damage at Hydrogenated Amorphous/Crystalline Silicon Interfaces by Indium Tin Oxide Overlayer Sputtering. *Appl. Phys. Lett.* **2012**, *101* (17), 171604.
- (38) Qiu, D.; Duan, W.; Lambertz, A.; Eberst, A.; Bittkau, K.; Rau, U.; Ding, K. Transparent Conductive Oxide Sputtering Damage on Contact Passivation in Silicon Heterojunction Solar Cells with Hydrogenated Nanocrystalline Silicon. *Sol. RRL* **2022**, *6* (10), 1–9.
- (39) Morales-vilches, A.; Voz, C.; Colina, M.; López, G.; Martín, I.; Ortega, P.; Orpella, A. Recovery of Indium-Tin-Oxide/Silicon Heterojunction Solar Cells by Thermal Annealing. *Energy Procedia* **2014**, *44*, 3–9.
- (40) Rißland, S.; Breitenstein, O. Considering the Distributed Series Resistance in a Two-Diode Model. *Energy Procedia* **2013**, *38*, 167–175.
- (41) Schulze, T. F.; Korte, L.; Conrad, E.; Schmidt, M.; Rech, B. Electrical Transport Mechanisms in A-Si:H/c-Si Heterojunction Solar Cells. *J. Appl. Phys.* **2010**, *107* (2), No. 023711.
- (42) Procel, P.; Xu, H.; Saez, A.; Ruiz-Tobon, C.; Mazzarella, L.; Zhao, Y.; Han, C.; Yang, G.; Zeman, M.; Isabella, O. The Role of Heterointerfaces and Subgap Energy States on Transport Mechanisms in Silicon Heterojunction Solar Cells. *Prog. Photovoltaics Res. Appl.* **2020**, *28* (9), 935–945.
- (43) Balent, J.; Smole, F.; Topic, M.; Krc, J. Numerical Analysis of Selective ITO/a-Si:H Contacts in Heterojunction Silicon Solar Cells: Effect of Defect States in Doped a-Si:H Layers on Performance Parameters. *IEEE J. Photovoltaics* **2021**, *11* (3), 634–647.